Electronic topology with bound defect charges promotes intermediate hexatic phase in two-dimensional melting

Junyan Ma [1,*] and H. Huang [1,2,3,†]

[1]*School of Physics, Peking University, Beijing 100871, China*
[2]*Collaborative Innovation Center of Quantum Matter, Beijing 100871, China*
[3]*Center for High Energy Physics, Peking University, Beijing 100871, China*

Disclinations play an amusing role in topological electronic states because of the ability to trap charges residing in the cores of these defects. According to the Kosterlitz-Thouless-Halperin-Nelson-Young (KTHNY) theory of two-dimensional (2D) melting, unbinding the bound pairs of disclinations (i.e., dislocations) induces the structural transition from the hexatic to liquid phase, corresponding to the destruction of quasilong range order. In this work, we elucidate the interplay between topological electronic states and the KTHNY structural transition. We verify the existence of electronic topology-induced charges that are trapped at disclinations during the 2D melting of hard disk particles. Resorting to the Ewald technique, we calculate the real-space distribution of the electrostatic potential generated by nonuniform Coulomb gas composed of these trapped charges. We found that the nonzero gradient of the electrostatic potential gives rise to additional contributions to the hydrostatic pressure. Based on the linear elastic theory, we further show that the electronic topology-induced trapped charges add extra contributions to the core energy of dislocations, increase the energy barrier of dislocation unbinding, and eventually decrease the lower critical boundary of the hexatic phase in the phase diagram. Our finding not only gives a special perspective for studying amorphous topological insulators but proposes a new impacting mechanism in the deviation of the phase boundary of structural transitions.

I. INTRODUCTION

The discovery of topological states of matter [1–3] gives a brand-new perspective for researchers to reexamine bountiful physical properties [4,5]. The attractive story takes its source from the discovery of the integer quantum Hall effect in the ultrastrong magnetic field [6], featuring the Hall plateau and characterized by the first Chern number [7]. Quantum spin Hall effect [8,9] is another famous example of topological states that are protected by time-reversal symmetry and characterized by the Z_2 topological invariant. Later, Fu proposed the concept of topological crystalline insulators where delicate topological bands are protected by spatial symmetries [10]. In recent years, higher-order topology, portrayed by lower-dimensional localized boundary states, has evoked immense attraction [11] and is experimentally realized in artificial devices, such as phononic crystals [12,13]. Going beyond the limitation of crystalline solids, efforts have been made to extend the territory of topological materials to disorder systems and quasicrystals [14–19]. The quantized conductance induced by disorder in topological Anderson insulators [20,21] and the robust bound states localized at corners of higher-order topological Anderson insulators [22] suggest that various novel properties emerging from the

interplay between electronic topology and structural disorders remain to be explored.

Thermodynamic fluctuations play a significant role in low dimensions [23]. A typical example is that the phase transition of 2D melting conflicts with Landau's paradigm [24]. The Kosterlitz-Thouless-Halperin-Nelson-Young (KTHNY) theory [25–28], supported by a series of numerical verifications [29] and experiments [30,31], has convincingly solved the controversy about the impossibility of long-range order in 2D melted solids [32]. Different from the single-stage first-order solid-liquid transition in 3D, the evolution from solid to liquid in 2D will pass through a two-step continuous transition via an intermediate state called hexatic phase [29,33–35], which maintains the quasilong range orientational order but collapses the translational order. When experiencing 2D melting, topological defects, denoted as vortices or disclinations, are gradually proliferating in the entire space [33,36]. According to the KTHNY theory, positional ordering is destroyed by the free dislocations made up of bound pairs of disclinations even in zero-temperature limits, meaning that the system goes into the hexatic phase. Then continuously heating crystals will additionally unbind these bound pairs of disclinations and drive the 2D system from the hexatic to liquid phase by degrees. In this process, the dimensionless Frank's constant F_A, which describes the interactions between the disclinations, converges to $72/\pi$ after separating all dislocations [27].

Thus, the behavior of disclinations determines the criticality of the KTHNY-type transition. We notice that, except in this respect of structural transformations, those geometric

*Corresponding author: junyan_ma@pku.edu.cn
†Corresponding author: huaqing.huang@pku.edu.cn

vortices also can trap a certain amount of charges in the presence of nontrivial band topology [37–40]. It is, therefore, natural to raise several questions. First, do these trapped charges still exist robustly when they interact with each other in the processing of melting? If so, how do the topologically trapped charges affect the 2D melting transition? Can we bridge two distinctive types of topological transitions by figuring out the implicit relationship between electronic band topology and geometric critical phenomena?

In this work, we excavate the underlying connection between band topology and the melting transition in two dimensions. Specifically, we first construct amorphous hexatic networks characterized by quasilong range ordering and solve the disordered topological model within them. Then, we analyze the real-space distribution of electrons and find that the nontrivial topological invariant endows disclinations, typically shown in pairs in the hexatic phase, with the ability to trap an amount of charges. By employing the Ewald summation method in two dimensions, we further evaluate the electrostatic potential formed by the nonuniform Coulomb gas composed of the trapped charges. We show that the fluctuation of the electrostatic potential leads to additional contributions to the hydrostatic pressure. To unearth the consequence of nonuniform Coulomb gas to the 2D melting transition, we calculate the core energy $\mathcal{E}_c$ of dislocations based on the linear elastic theory. We show that $\mathcal{E}_c$ obtains an additional contribution from the electronic topology-induced trapped charges. This implies the increase of the energy barrier to breaking the bound pairs of disclinations, which lowers the critical boundary of the hexatic phase according to the KTHNY theory of 2D melting.

II. MELTING OF HARD DISKS IN TWO DIMENSIONS

We use the event-chain Monte Carlo algorithm [34] to thermalize those hard disk particles in the NVT ensemble adopting the periodic boundary condition (PBC) in two vertical directions. We set the total displacement [41] in this algorithm $\xi = 5\sigma$ where σ is the radius of the particle. The number of Monte Carlo steps is set to 2×10^4 to fully reach the equilibrium (see the Supplemental Material (SM) [42]). Particle density $\rho = \frac{N\pi\sigma^2}{\Omega}$ is the only independent variable of the simulation of hard-disk melting, where N and Ω are the number of particles and the volume of a supercell, respectively. The local bond orientational function is defined as $\psi_{6,i} = \frac{1}{n}\sum_{(k,i)} e^{i6\theta_{ki}}$, where n assigns the coordination number of the site i, and θ_{ki} is the relative angle between the bond connecting site pair (k, i), and the axis of the horizontal direction. $\psi_{6,i}$ is equal to one in the fully crystalline arrangement. Due to fluctuations, a useful observable is the correlation of bond orientational functions $g_6(r)$, defined as $g_6(r) = \langle \tilde{\psi}_{6,i}\psi_{6,j}\delta(r - r_{ij})\rangle$, where the tilt represents complex conjugate and $\langle \cdot \rangle$ denotes the thermodynamic average. We consider over 1.2×10^5 disks in a supercell and calculate $g_6(r)$ to find the hexatic-liquid geometric phase boundary. As shown in Fig. 1(a), the exponential decay of correlation functions around $\rho = 0.65$ indicates the lower bounds of the density ρ for the hexatic phase. We also verify that the quasilong range bond-orientational ordering remains as long as $\rho > 0.65$ because the exponent of the orientational function

$g_6(r)$ is larger than $-1/4$, which is the lower limit for a hexatic phase in the continuous KTHNY transition [34,43]. Our results are consistent with previous studies [44].

III. AMORPHOUS TOPOLOGICAL MODEL

Having obtained amorphous structures maintaining bond orientational ordering, we further construct a general tight-binding model based on a triple atomic basis (s, p_x, p_y) on each site in the network generated by Delaunay triangulation [45] according to the spatial pattern of sites (see the SM [42] for details) and the intersite hoppings are denoted by the edges of these triangles, as shown in Fig. 1(b). Due to the limited computational resources, we randomly select a finite region containing $N = 768$ atoms in the entire area for the tight-binding calculations. The Hamiltonian of the model is expressed as [19]:

$$H = \sum_{i\alpha} \omega_\alpha c_{i\alpha}^\dagger c_{i\alpha} + \sum_{\langle i\alpha, j\beta \rangle} t_{i\alpha, j\beta} c_{i\alpha}^\dagger c_{j\beta}$$
$$+ i\lambda_{so} \sum_i \left(c_{ip_y}^\dagger \tau_z c_{ip_x} - c_{ip_x}^\dagger \tau_z c_{ip_y} \right), \tag{1}$$

where $c_{i\alpha} = (c_{i\alpha\uparrow}, c_{i\alpha\downarrow})$ are electron annihilation operators on the orbits α $(= s, p_x, p_y)$ at site i, ω_α is the on-site energy of the orbit α, λ_{so} is the strength of the spin-orbit coupling (SOC), and τ_z is the Pauli matrix. The second term is the nearest-neighbor hoppings which are represented by red lines in Fig. 1(b). The hopping integral between orbital α and β are determined by Slater-Koster approximations [46]: $t_{i\alpha, j\beta} = t_{\alpha,\beta}(\mathbf{d}_{ij}) = \mathrm{SK}[T_{\alpha\beta}/d_{ij}^2, \hat{\mathbf{d}}_{ij}]$, where $\mathbf{d}_{ij} = \mathbf{r}_i - \mathbf{r}_j = d_{ij}\hat{\mathbf{d}}_{ij}$ and $T_{\alpha\beta}$ are bond parameters which are chosen to have an inverse-square decay with the distance d_{ij} [47]. Because the band inversions triggering topological phase transitions (TPT) occur between s and p orbitals with different parities, we assume two thirds of eigenstates of Eq. (1) are occupied.

IV. TRAPPED CHARGES RESIDING IN THE CORE OF DISCLINATION

We first verify the topological state in the hexatic lattice with $\rho = 0.7$ by directly calculating the spin Bott index B_s [48]. As shown in Fig. 1(c), a topological phase transition between a normal insulator ($B_s = 0$) and a quantum spin Hall (QSH) state ($B_s = 1$) occurs at $\lambda_{so} \approx 1.15$ eV. Moreover, topological edge modes appear in the QSH state which coincides with that in crystalline lattices [42]. Then, we analyze the exact amount of electric charges on each site in both topological and normal states. In principle, all states below the Fermi level are occupied by electrons around these sites in the network, thus every occupied state contributes to the total charges of the system. The distribution of the modulus square of the wave function $|\Psi(\mathbf{r})\rangle$ indicates the probability of finding electrons at $\mathbf{r}$, which is in proportion to the accumulation of electronic charges in real space. In our calculation, the amount of the total positive charge is normalized to one. Figure 1(c) shows the averaged amount of trapped charge in two types of disclinations, which are topological defects composed of pentagons or heptagons and are denoted by
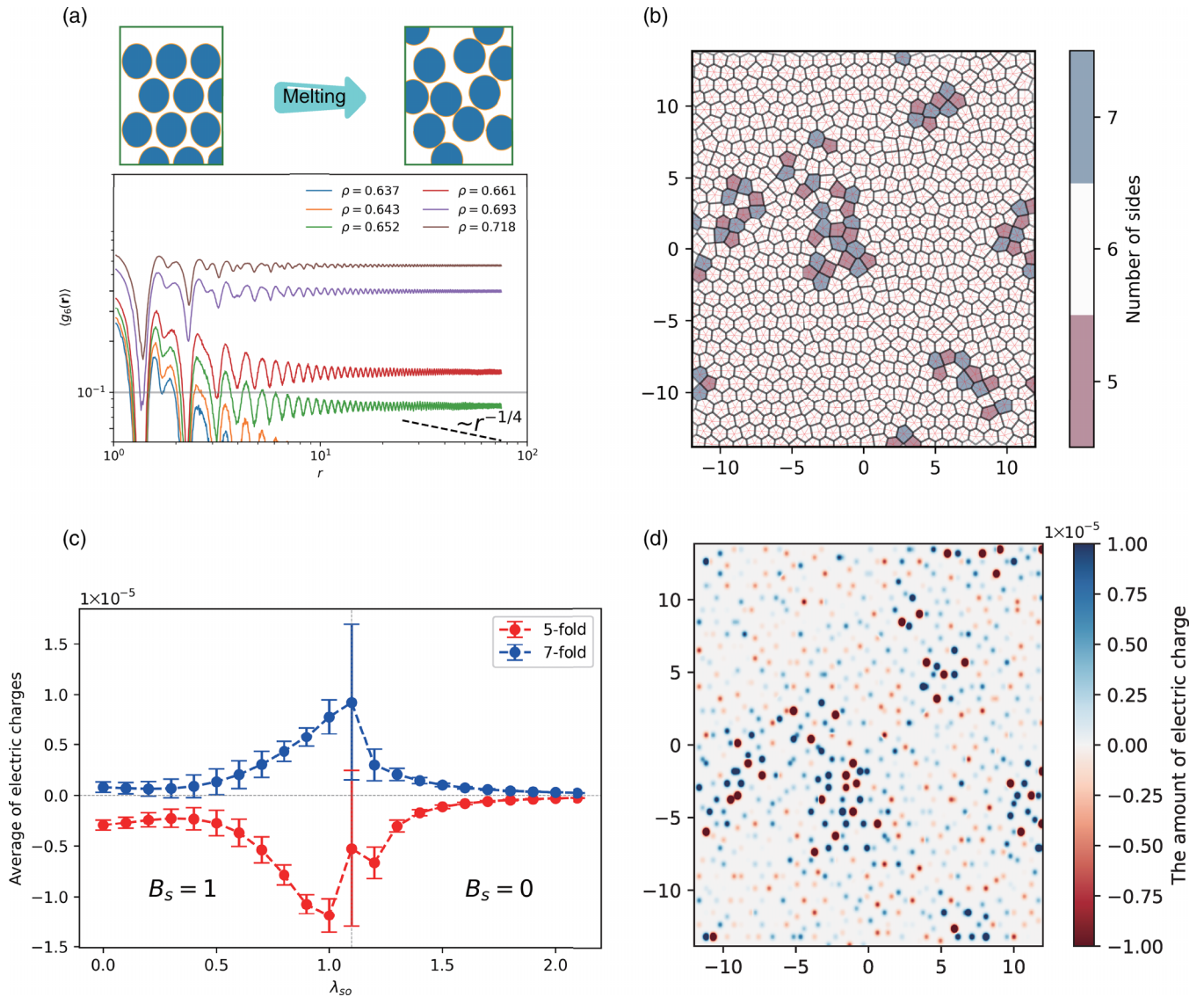
FIG. 1. The electric charges are trapped in the topological vortices during 2D melting. (a) Schematic display of melting of hard disks and the bond-orientational correlation functions $g_6(r)$. The slope of the black dashed line in (a) is $-1/4$, which equals the minimum possible slope for a hexatic phase. (b) The tight-binding model containing 768 melting disks is based on Delaunay triangulation (denoted by thin red lines) with the periodic boundary condition (PBC). The polygons marked by black lines are the Voronoi cells where atomic sites are located in the center of each cell and the intersite hoppings are represented by the edges of Delaunary triangles (i.e., the thin red lines). (c) The average of electric charges according to different types of topological defects in the hexatic lattice with $\rho = 0.7$. Over 20 realizations are considered in the calculation. The horizontal black dashed line stands for zero value, while the vertical one is the location of the topological transition of the amorphous topological model. (d) The real-space distribution of electric charges and the color bar represents the amount of charges. The fixed parameters used for calculations in (c) and (d) are $\omega_s = 0.18$, $\omega_p = -0.65$, $T_{ss\sigma} = -0.04$, $T_{sp\sigma} = 0.09$, $T_{pp\sigma} = 0.18$, and $T_{pp\pi} = 0.05$ eV.

topological charge $Q = -1$ and $Q = +1$, respectively. Despite different decay behaviors of the trapped charge on opposite sides of the critical point, disclinations do trap some charges in both topologically trivial and nontrivial states. Specifically, as long as SOC is relatively close to the critical point ($0.6 \leqslant \lambda_{so} \leqslant 1.3$), disclinations remain effectively trapping considerable charges on the order of $10^{-5}e$ in the hexatic lattice. However, distinctive from isolated defects that trap a fixed value of charges, the trapped charges of disclinations fluctuate in the hexatic lattice where the separations between disclinations vary locally. Nevertheless, we note that

disclinations with $Q = \pm 1$ seize comparable negative and positive charges, ensuring the electric neutrality of sixfold sites. In addition, we also examine the trapped charge of the dislocation which is composed of a bound pair of disclinations with $Q = \pm 1$. We verified that two isolated dislocations with large distances can capture charge dipoles [42]. Previous research reports the liquid-hexatic coexistence phase where dislocations and disclinations coexist and nonuniformly distribute in the system [34]. Therefore, the electronic topology would induce a nonuniform distribution of lattice Coulomb gas in the melting structure, as illustrated in Fig. 1(d).
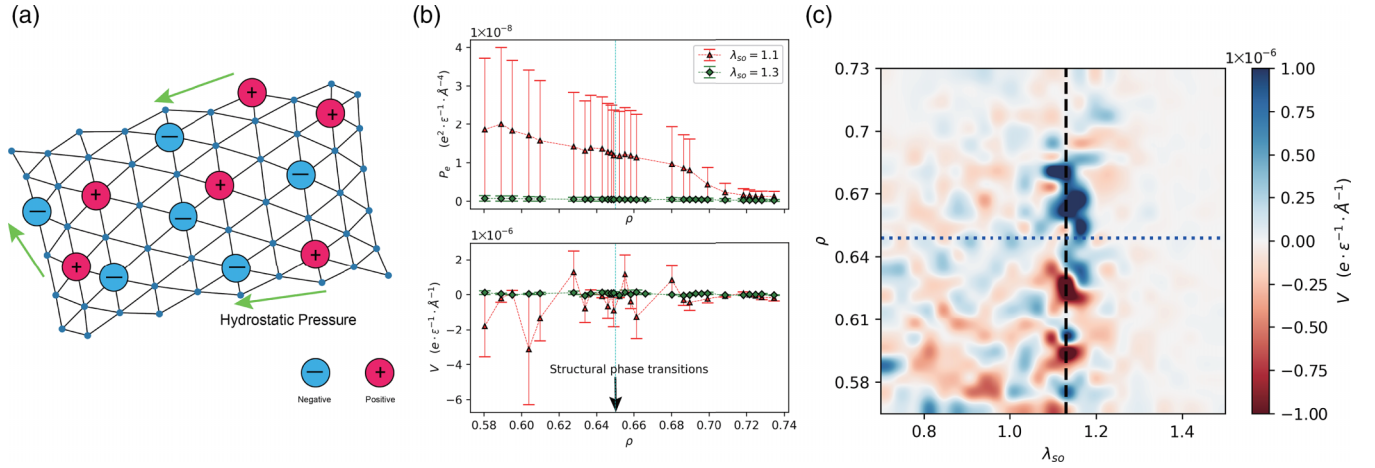
FIG. 2. The hydrostatics of the network stem from the trapped electrons on the site. (a) Sketch of the net charges in the disordered triangular lattice. (b) The electrostatic pressure P_e and potential V as the functions of particle density ρ, where 20 realizations are considered. The dashed vertical cyan line denotes the critical density $\rho = 0.65$. $\lambda_{so} = 1.1$ and 1.3 eV are assigned topological and trivial phases of the amorphous tight-binding model defined as Eq. (1), respectively. (c) Phase diagram of electrostatic potential V. The horizontal dotted blue and vertical dashed black lines indicate the structural and topological transitions, respectively.

V. HYDROSTATICS STEMMING FROM LOCAL NON-NEUTRALITY

Having established the relationships between the nonuniform charge trapping around topological phase transition and disclination-involved structural evolution during 2D melting, it is natural to speculate that these induced charges residing in the amorphous hexatic network will form a nonuniform electric field. As shown in Fig. 2(a), we anticipate the existence of the nonzero hydrostatic pressure P_e originating from trapped charges on the local defect sites. To figure that out, we first calculate the electrostatic potential $V(\mathbf{r})$ by using the Ewald summation method which rewrites the long-range correlated potential as two parts $V_{s(l)}(\mathbf{r})$ to avoid the divergence. Explicitly, $V(\mathbf{r})$ in 2D lattices is expressed as [49]

$$
\begin{aligned}
V(\mathbf{r}) &= V_s(\mathbf{r}) + V_l(\mathbf{r}) \\
&= \frac{1}{4\pi\varepsilon} \sum_{\mathbf{n}} \sum_{j=1}^{N} \frac{q_j}{|\mathbf{r} - \mathbf{r}_j + \mathbf{n} \cdot \mathbf{a}|} \operatorname{erfc}\left(\frac{|\mathbf{r} - \mathbf{r}_j + \mathbf{n} \cdot \mathbf{a}|}{\sqrt{2}\mu} \right) \\
&\quad + \frac{1}{2|\mathbf{a}_1||\mathbf{a}_2|\varepsilon} \sum_{\mathbf{k} \neq \mathbf{0}} \sum_{j=1}^{N} \frac{q_j}{|\mathbf{k}|} e^{i\mathbf{k}\cdot(\mathbf{r}-\mathbf{r}_j)} \operatorname{erfc}\left(\frac{|\mathbf{k}|\mu^2}{2} \right).
\end{aligned}
\tag{2}
$$

Here, the subscripts s and l represent the short and long-range parts of total potential, respectively. q_j is the amass of electric charges at site j and erfc() represents the complementary error function. μ is the spread of localized electronic distribution and we set $\mu = 0.25$ (i.e., a quarter of the averaged inter-site distance), $\mathbf{a} = (\mathbf{a_1}, \mathbf{a_2})$ with $\mathbf{a}_{1(2)}$ being two orthogonal lattice vectors of the supercell, and $\mathbf{k}$ the reciprocal vectors. $\mathbf{n} = (n_1, n_2)$ represents the number of supercells in two vertical directions. After obtaining $V(\mathbf{r})$, we can further calculate the Maxwell stress tensor

$$
\eta_{ij} = \varepsilon E_i E_j - \frac{1}{2}(\varepsilon E_i E_j \delta_{ij}),
\tag{3}
$$

where electric field $\mathbf{E} = (E_x, E_y)$ is the gradient of $V(\mathbf{r})$, and ε is the permittivity of materials. Then, the hydrostatic pressure is given by [50]

$$
P_e(\mathbf{r}) = \frac{1}{2}(\eta_{xx} + \eta_{yy}).
\tag{4}
$$

Due to the local spatial fluctuation of $P_e(\mathbf{r})$ and $V(\mathbf{r})$, we evaluate the spatial average of the hydrostatic pressure $\overline{P_e(\mathbf{r})}$ and the electrostatic potential $\overline{V(\mathbf{r})}$. For amorphous hexatic structures at each ρ, we further perform configuration averages on these quantities over 20 realizations, which yield $P_e = \langle \overline{P_e(\mathbf{r})} \rangle$ and $V = \langle \overline{V(\mathbf{r})} \rangle$.

Figure 2(b) shows the averaged hydrostatic pressure P_e and electrostatic potential V as functions of particle density ρ. For comparison, we chose $\lambda_{so} = 1.1$ and 1.3 eV, which belong to different topological phases. A pronounced P_e is found in the topological phase at $\lambda_{so} = 1.1$ eV, while P_e is nearly zero in the trivial phase at $\lambda_{so} = 1.3$ eV. This implies that electronic topology indeed leads to an extra contribution to hydrostatic pressure as the topological phase exhibits a stronger ability to trap charges at disclinations. Moreover, P_e decreases gradually with increasing ρ and vanishes rapidly when ρ is approaching 0.69. The reason can be attributed to the accompaniment which is a decrease in the number of topological defects and a decrement of trapped charge at each defect, as exhibited in Fig. 3(a). The behavior of P_e can also be understood from the evolution of the electrostatic potential V. As shown in the bottom panel of Fig. 2(b), the averaged V exhibits violent fluctuations with large error bars when $\rho < 0.65$ and $\lambda_{so} = 1.1$ eV. This indicates that the nontrivial electronic topology-induced nonuniformed Coulomb gas in the amorphous network generates inhomogeneous electrostatic potential $V(\mathbf{r})$ and nonzero electric field $\mathbf{E}$, which eventually yields a significant contribution of P_e.

We further calculate the phase diagram of V in the (λ_{so}, ρ) plane to explicitly exhibit the physical origins of P_e. As shown in Fig. 2(c), the averaged electrostatic potential exhibits strong fluctuations around the topological phase transition at $\lambda_{so} \approx$ 1.15 eV since the disclinations trap a significant amount of
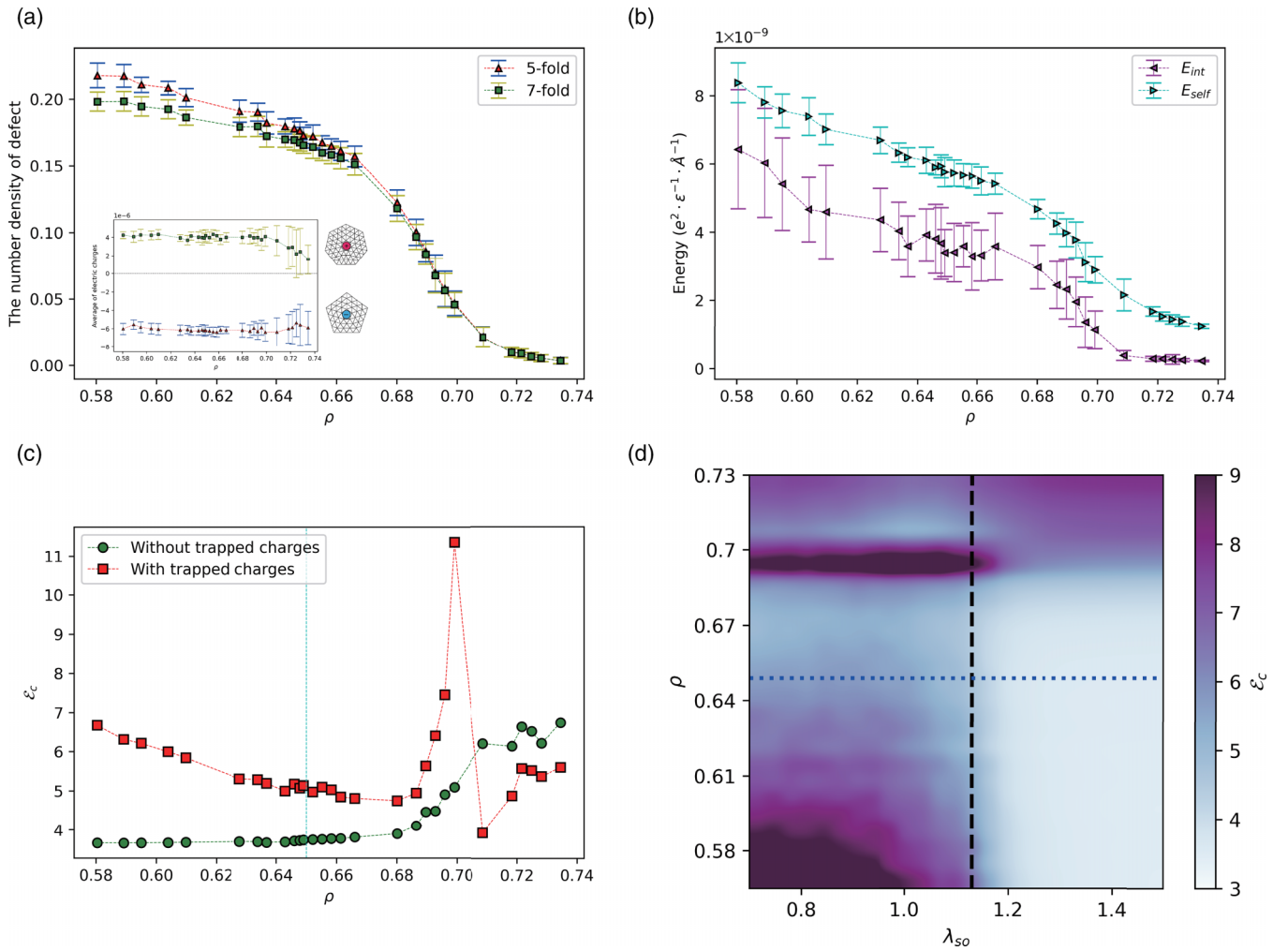
FIG. 3. Summaries about charged topological defects and their impact on structural transitions, originating from nontrivial topological bands. (a) The number density of two types of disclinations as the functions of ρ, and the inset shows their average of electric charges compulsively localized in the defect core. (b) The electrostatic interaction E_{int} and self-energies E_{self} of the entire system, with their corresponding values depending on the particle densities. (c) The core energy of dislocation $\mathcal{E}_c$ as the functions of ρ. The red and green dashed lines represent the $\mathcal{E}_c$ whether considering electrostatic force, respectively. (d) Phase diagram of $\mathcal{E}_c$ in the (λ_{so}, ρ) plane. The meaning of the horizontal dotted blue and vertical dashed black lines is the same as that in Fig. 2(c).

charges near the critical point as illustrated in Fig. 1(c). Moreover, we note that the undulating distribution of V is evident in the left lower region (i.e., $\rho < 0.65$ and $\lambda_{so} < 1.15$ eV) but diminishes in other regions. This is also attributed to the decrease in the number of disclinations and the trapped charges at each defect when $\rho > 0.65$ or $\lambda_{so} > 1.15$ eV.

VI. DEVIATIONS OF DISCLINATION-INDUCING CRITICALITY

Next, we analyze the effect of electronic topology on the 2D melting. In a microscopic perspective, the 2D melting transition is determined by the free energy of topological defects $\mathcal{F}_c = \mathcal{E}_c - \mathcal{T}\mathcal{S}_c$, where $\mathcal{S}_c$ is the entropy depending on structural configurations while $\mathcal{E}_c$ can be assigned as the formation energy of dislocations or disclinations. Macroscopically, the nonuniform locally trapped charges will exert the electrostatic forces in the network and change the elastic modulus. We, therefore, expect that the critical behaviors of 2D melting

would be modified around the topological phase transition of electronic structures.

We first display the number densities of five and sevenfold disclinations and their trapped charges as shown in Fig. 3(a). The number densities of disclinations increase with decreasing the particle density ρ. In particular, they undergo a rapid surging when ρ changes from 0.70 to 0.65. Apart from that, we also note that a discrepancy in the number density of the two types of disclinations appears at low particle density when the hexatic structure with orientational ordering falls apart, meaning the complete decoupling of dislocation and the formation of other types of defects (see Fig. S2(e) and Fig. S9 for details [42]). As shown in the inset of Fig. 3(a), the average of trapped charges for both types of disclinations remains almost unchanged until ρ goes to quite ordered phase (i.e., $\rho > 0.7$). Specifically, the charge trapped by both types of disclinations decreases when $\rho > 0.65$ as the system enters the hexatic phase with relatively small numbers of disclinations.

Second, we delve into the electrostatic energy induced by trapped electrons. Specifically, we calculate the electrostatic interaction energy $E_{int} = \frac{1}{2} \sum_i^N q_i V(\mathbf{r_i})$ and the self-energy [49] $E_{self} = \frac{1}{4\sqrt{2}\pi^{\frac{3}{2}} \varepsilon \mu} \sum_{i=1}^N q_i^2$, where $\mathbf{r}_i$ is the position of site i with a trapped charge q_i. Since the trapped charges are mainly originated from five and sevenfold disclinations, the electrostatic energies E_{int} and E_{self} [as shown in Fig. 3(b)] exhibit a similar dependence on ρ as the number density exhibited in Fig. 3(a). In addition, we note that the hydrostatic pressure P_e in the topological states [as shown in the top panel of Fig. 2(b)] also shares a similar trend as the electrostatic energies and the number density. These results lend additional support to the conclusion that the number of disclinations and the electronic topology-induced trapped charges on these defects determine the extra electrostatic energy and hydrostatic pressure.

Third, we study the modification of the elastic properties of the 2D system due to electrostatic interaction. We specifically focus on Young's modulus K which is not only the mechanical properties of materials but also related to the core energy of dislocations $\mathcal{E}_c$ [33]. We treat electrostatic effects in the framework of linear elasticity [51], i.e., Hooke's law,

$$\eta_{ij} = \hat{C}_{ijkl} \epsilon_{kl}, \tag{5}$$

where ϵ_{kl} is the strain tensor. The total elastic matrix consists of force originating from hard-core potential and electrostatics, which can be expressed as

$$\hat{C} = \hat{C}_h + \hat{C}_e, \tag{6}$$

where the subscripts h and e refer to hard-core potential and electrostatics, respectively. The Young's modulus can be obtained from the matrix form of $\hat{C}_{ijkl}$ directly via a linear association that $K = \frac{1}{4}(C_{11} + C_{22} + 2C_{12})$ [52] in the hexagon, where $C_{11} = C_{1111}$, $C_{12} = C_{1122}$ and $C_{22} = C_{2222}$ in Voigt notations and further can be restricted $C_{11} = C_{22}$ in triangular network [42]. We evaluate the $\hat{C}_h$ according to the strain fluctuation[53], $\langle \Delta\epsilon_{ij}\Delta\epsilon_{kl} \rangle = (kT/\Omega)(\hat{C}_h)^{-1}_{ijkl}$. Having obtained the elastic modulus, we can determine the core energy $\mathcal{E}_c$ of a single dislocation (i.e. a bound pair of disclinations) [54],

$$\mathcal{E}_c = \frac{kT}{2}\left\{ \ln\left[\frac{2\pi\sqrt{3}}{K/8\pi - 1}I_0\left(\frac{K}{8\pi}\right)\right] + \frac{K}{8\pi} - \ln(p_d) \right\}, \tag{7}$$

where p_d is the density of dislocation which approximately equals the average of 5-fold and 7-fold disclinations and I_0 is the zero-order Bessel function.

We exhibit the core energy of dislocation as the function of ρ in Fig. 3(c). Here, we compare $\mathcal{E}_c$ of the hard-disk system before and after considering the electrostatics. Since liquid states cannot be squeezed or stretched, the elastic modulus will disappear and linear elasticity fails. However, we formally calculate elastic energy even in quite disordered phases (where ρ is small) according to Eq. (6). For the case without considering the trapped charges, $\mathcal{E}_c$ which solely stem from hard-core potential, decreases along with the decreasing ρ and gradually converges to a constant (≈ 3.6) after ρ below the critical point ($\rho = 0.65$), consistent with previous works [54]. However, the situation becomes complicated when the trapped charges are considered. In the heaxtic phase far above

the critical point ($\rho \gg 0.65$), the trapped charges diminish $\mathcal{E}_c$. As ρ approaches 0.7, a striking peak of $\mathcal{E}_c$ emerges after considering the electrostatics of trapped charges. In contrast, for liquid phase ($\rho < 0.65$), $\mathcal{E}_c$ increases gradually with decreasing ρ. Physically, the weak contribution of trapped charges in the ordered phase with large ρ is mainly due to the lack of topological defects. However, near the hexatic-liquid phase transition, the rapidly increasing rate of number density of defects makes electricity play the dominant role, which implies that the total amount of trapped charges determines $\mathcal{E}_c$ near the phase transitions.

To further study the effect of amorphous topological states on structural phase transition, we calculate the phase diagram of $\mathcal{E}_c$ in the (λ_{so}, ρ) plane, as shown in Fig. 3(d). We first note the existence of distinct discontinuity when $\rho \approx 0.7$ and $\lambda_{so} < 1.15$ eV, implying that trapped charges make considerable contributions to dislocation energy. In the topological phase ($\lambda_{so} < 1.15$ eV), $\mathcal{E}_c$ increases at the decrease of ρ, because disclinations can accommodate more charges. However, the topologically trivial region ($\lambda_{so} > 1.15$ eV) is impervious from the effect of electronic states, due to the defect quickly losing the ability to trap charges.

Because the dislocation energy $\mathcal{E}_c$ is also related to the Frank constant

$$F_A = 2\mathcal{E}_c r_c^2, \tag{8}$$

that characterizes the interaction between disclinations [31], where r_c is the radius of dislocations. Thus, we should reassess the F_A because of the additional contributions from nontrivial electrostatics. Physically, the criterion that determines the boundary of hexatic-liquid phase transition is the reach of the infinity of the radius r_c (i.e., the dislocation fully falls apart), which gives [27]

$$\rho F_A \rightarrow \text{const.} \tag{9}$$

The r_c is the same for two different cases with and without considering the trapped charges, due to the share of the same geometric structure. Therefore, $\mathcal{E}_c$ determines the deviation of phase boundary from the original 2D melting transition.

As shown in Fig. 3(d), due to the higher $\mathcal{E}_c$ in the topological region, the critical density should reduce according to Eq. (9). In other words, the range of the intermediate hexatic phase should expand after considering the electronic topology-induced trapped charges. In the presence of nontrivial electronic topological states, it requires stronger thermal excitation for 2D melting systems to counteract the additional electricity from trapped charges. We also notice that those extra contributions continue to increase as the density ρ further decreases in the more disordered liquid phase. Since our calculations are based on linear elasticity which is not valid for liquid, the behavior of $\mathcal{E}_c$ in the liquid phase is no longer physically meaningful.

VII. CONCLUSIONS

We reported a role of electronic topology in 2D melting transitions, which are delineated according to KTHNY theory. We constructed the hexatic structure characterized by the algebraic decay of bond orientational function $g_6(r)$ and verified the existence of trapped charges at disclinations when

the system is in the nontrivial electronic topological state. To further study the concrete impact of trapped charges on the KTHNY-type transitions, we use the Ewald summation method to calculate the electrostatic potential generated by the trapped Coulomb gas in two dimensions. It is found that the fluctuation of the electrostatic potential leads to additional contributions to the hydrostatic pressure. We also delved into the elasticity of the system based on linear elastic theory and found the deviation of structural criticality of structural transition. Specifically, the electronic topology-induced trapped charges make additional contributions to the core energy of dislocation when the system experiences the hexatic-liquid phase transition. Thus, it broadens the range of the hexatic phase by extending its lower critical boundary. Our work exposed an underlying physical connection between 2D melting transitions and the electronic topology.

[1] M. Z. Hasan and C. L. Kane, *Colloquium:* Topological insulators, Rev. Mod. Phys. **82**, 3045 (2010).

[2] X.-L. Qi and S.-C. Zhang, Topological insulators and superconductors, Rev. Mod. Phys. **83**, 1057 (2011).

[3] A. Bansil, H. Lin, and T. Das, *Colloquium:* Topological band theory, Rev. Mod. Phys. **88**, 021004 (2016).

[4] J. Hu, S.-Y. Xu, N. Ni, and Z. Mao, Transport of topological semimetals, Annu. Rev. Mater. Res. **49**, 207 (2019).

[5] D. Culcer, A. C. Keser, Y. Li, and G. Tkachov, Transport in two-dimensional topological materials: recent developments in experiment and theory, 2D Mater. **7**, 022007 (2020).

[6] K. v. Klitzing, G. Dorda, and M. Pepper, New method for high-accuracy determination of the fine-structure constant based on quantized Hall resistance, Phys. Rev. Lett. **45**, 494 (1980).

[7] D. J. Thouless, M. Kohmoto, M. P. Nightingale, and M. den Nijs, Quantized Hall conductance in a two-dimensional periodic potential, Phys. Rev. Lett. **49**, 405 (1982).

[8] C. L. Kane and E. J. Mele, Quantum spin Hall effect in graphene, Phys. Rev. Lett. **95**, 226801 (2005).

[9] C. L. Kane and E. J. Mele, Z_2 topological order and the quantum spin Hall effect, Phys. Rev. Lett. **95**, 146802 (2005).

[10] L. Fu, Topological crystalline insulators, Phys. Rev. Lett. **106**, 106802 (2011).

[11] B. Xie, H.-X. Wang, X. Zhang, P. Zhan, J.-H. Jiang, M. Lu, and Y. Chen, Higher-order band topology, Nat. Rev. Phys. **3**, 520 (2021).

[12] H.-X. Wang, Q. Wang, K.-G. Zhou, and H.-L. Zhang, Graphene in light: Design, synthesis and applications of photo-active graphene and graphene-like materials, Small **9**, 1266 (2013).

[13] M. Serra-Garcia, V. Peri, R. Süsstrunk, O. R. Bilal, T. Larsen, L. G. Villanueva, and S. D. Huber, Observation of a phononic quadrupole topological insulator, Nature (London) **555**, 342 (2018).

[14] S. Mansha and Y. D. Chong, Robust edge states in amorphous gyromagnetic photonic lattices, Phys. Rev. B **96**, 121405(R) (2017).

[15] J. Ma and H. Huang, Amorphous Kane-Mele model in disordered hyperuniform two-dimensional networks, Phys. Rev. B **106**, 195150 (2022).

[16] A. Agarwala and V. B. Shenoy, Topological insulators in amorphous systems, Phys. Rev. Lett. **118**, 236402 (2017).

[17] C. Wang, T. Cheng, Z. Liu, F. Liu, and H. Huang, Structural amorphization-induced topological order, Phys. Rev. Lett. **128**, 056401 (2022).

[18] X. Ni, H. Huang, and F. Liu, Robustness of topological insulating phase against vacancy, vacancy cluster, and grain boundary bulk defects, Phys. Rev. B **101**, 125114 (2020).

[19] H. Huang and F. Liu, Quantum spin Hall effect and spin Bott index in a quasicrystal lattice, Phys. Rev. Lett. **121**, 126401 (2018).

[20] J. Li, R.-L. Chu, J. K. Jain, and S.-Q. Shen, Topological Anderson insulator, Phys. Rev. Lett. **102**, 136806 (2009).

[21] C. W. Groth, M. Wimmer, A. R. Akhmerov, J. Tworzydło, and C. W. J. Beenakker, Theory of the topological Anderson insulator, Phys. Rev. Lett. **103**, 196805 (2009).

[22] A. Agarwala, V. Juričić, and B. Roy, Higher-order topological insulators in amorphous solids, Phys. Rev. Res. **2**, 012067(R) (2020).

[23] M. Kardar, *Statistical Physics of Fields* (Cambridge University Press, Cambridge, 2007).

[24] L. D. Landau, On the theory of phase transitions, Zh. Eksp. Teor. Fiz. **7**, 19 (1937).

[25] J. M. Kosterlitz and D. J. Thouless, Long range order and metastability in two dimensional solids and superfluids. (Application of dislocation theory), J. Phys. C **5**, L124 (1972).

[26] B. I. Halperin and D. R. Nelson, Theory of two-dimensional melting, Phys. Rev. Lett. **41**, 121 (1978).

[27] D. R. Nelson and B. I. Halperin, Dislocation-mediated melting in two dimensions, Phys. Rev. B **19**, 2457 (1979).

[28] A. P. Young, Melting and the vector Coulomb gas in two dimensions, Phys. Rev. B **19**, 1855 (1979).

[29] A. Jaster, The hexatic phase of the two-dimensional hard disk system, Phys. Lett. A **330**, 120 (2004).

[30] J. Zanghellini, P. Keim, and H. H. von Grünberg, The softening of two-dimensional colloidal crystals, J. Phys.: Condens. Matter **17**, S3579 (2005).

[31] H.-H. von Grünberg, P. Keim, and G. Maret, Phase transitions in two-dimensional colloidal systems, in *Soft Matter*, edited by G. Gomppe and M. Schick (John Wiley & Sons, Ltd, 2007), Chap. 2, pp. 41–86.

[32] N. D. Mermin and H. Wagner, Absence of ferromagnetism or antiferromagnetism in one- or two-dimensional isotropic Heisenberg models, Phys. Rev. Lett. **17**, 1133 (1966).

[33] K. J. Strandburg, Two-dimensional melting, Rev. Mod. Phys. **60**, 161 (1988).

[34] E. P. Bernard and W. Krauth, Two-step melting in two dimensions: First-order liquid-hexatic transition, Phys. Rev. Lett. **107**, 155704 (2011).

[35] S. C. Kapfer and W. Krauth, Two-dimensional melting: From liquid-hexatic coexistence to continuous transitions, Phys. Rev. Lett. **114**, 035702 (2015).

[36] R. A. Quinn and J. Goree, Experimental test of two-dimensional melting through disclination unbinding, Phys. Rev. E **64**, 051404 (2001).

[37] Y. Liu, S. Leung, F.-F. Li, Z.-K. Lin, X. Tao, Y. Poo, and J.-H. Jiang, Bulk–disclination correspondence in topological crystalline insulators, Nature (London) **589**, 381 (2021).

[38] C. W. Peterson, T. Li, W. Jiang, T. L. Hughes, and G. Bahl, Trapped fractional charges at bulk defects in topological insulators, Nature (London) **589**, 376 (2021).

[39] T. Li, P. Zhu, W. A. Benalcazar, and T. L. Hughes, Fractional disclination charge in two-dimensional C_n-symmetric topological crystalline insulators, Phys. Rev. B **101**, 115115 (2020).

[40] S. Liu, A. Vishwanath, and E. Khalaf, Shift insulators: Rotation-protected two-dimensional topological crystalline insulators, Phys. Rev. X **9**, 031003 (2019).

[41] D. A. Levin, Y. Peres, and E. L. Wilmer, *Markov Chains and Mixing Times* (American Mathematical Society, 2006).

[42] See Supplemental Material at http://link.aps.org/supplemental/10.1103/PhysRevB.109.205107 for more details about the derivation and numerical calculations, which include Refs. [49,55–59].

[43] Y.-W. Li, Y. Yao, and M. P. Ciamarra, Two-dimensional melting of two- and three-component mixtures, Phys. Rev. Lett. **130**, 258202 (2023).

[44] W. Qi, A. P. Gantapara, and M. Dijkstra, Two-stage melting induced by dislocations and grain boundaries in monolayers of hard spheres, Soft Matter **10**, 5449 (2014).

[45] A. Okabe, B. Boots, K. Sugihara, and S. N. Chiu, *Spatial Tessellations: Concepts and Applications of Voronoi Diagrams*, 2nd ed., Series in Probability and Statistics (John Wiley and Sons, Inc., 2000).

[46] J. C. Slater and G. F. Koster, Simplified LCAO method for the periodic potential problem, Phys. Rev. **94**, 1498 (1954).

[47] W. Harrison, *Electronic Structure and the Properties of Solids : The Physics of the Chemical Bond* (Dover Publications, Mineola, New York, 1989).

[48] H. Huang and F. Liu, Theory of spin Bott index for quantum spin Hall states in nonperiodic systems, Phys. Rev. B **98**, 125130 (2018).

[49] F. E. Harris, Ewald summations in systems with two-dimensional periodicity, Int. J. Quant. Chem. **68**, 385 (1998).

[50] T. H. G. Megson, *Structural and Stress Analysis* (Butterworth-Heinemann, Boston, 2019).

[51] P. L. Gould and Y. Feng, *Introduction to Linear Elasticity*, 4th ed. (Springer, Cham, Switzerland, 2018).

[52] R. C. Andrew, R. E. Mapasha, A. M. Ukpong, and N. Chetty, Mechanical properties of graphene and boronitrene, Phys. Rev. B **85**, 125428 (2012).

[53] M. Parrinello and A. Rahman, Strain fluctuations and elastic constants, J. Chem. Phys. **76**, 2662 (1982).

[54] S. Sengupta, P. Nielaba, and K. Binder, Elastic moduli, dislocation core energy, and melting of hard disks in two dimensions, Phys. Rev. E **61**, 6294 (2000).

[55] E. P. Bernard, W. Krauth, and D. B. Wilson, Event-chain monte carlo algorithms for hard-sphere systems, Phys. Rev. E **80**, 056704 (2009).

[56] D. Abutbul and D. Podolsky, Topological order in an antiferromagnetic tetratic phase, Phys. Rev. Lett. **128**, 255501 (2022).

[57] M. J. Hytch, Analysis of variations in structure from high resolution electron microscope images by combining real space and fourier space information, Microsc. Microanal. Microstruct. **8**, 41 (1997).

[58] M. Michel, S. C. Kapfer, and W. Krauth, Generalized event-chain Monte Carlo: Constructing rejection-free global-balance algorithms from infinitesimal steps, J. Chem. Phys. **140**, 054116 (2014).

[59] M. Gonçalves, P. Ribeiro, R. Mondaini, and E. V. Castro, Temperature-driven gapless topological insulator, Phys. Rev. Lett. **122**, 126601 (2019).